PAPER • **OPEN ACCESS**

Three-dimensional modeling of Alkaline Water Electrolyzers

To cite this article: Federico Croci *et al* 2024 *J. Phys.: Conf. Ser.* **2893** 012063

Journal of Physics: Conference Series **2893** (2024) 012063 doi:10.1088/1742-6596/2893/1/012063

Three-dimensional modeling of Alkaline Water Electrolyzers

Federico Croci*[1], Alessandro d'Adamo[1], Nicolò Pavan[1], Ilario Cordisco[1]

Dipartimento di Ingegneria "Enzo Ferrari", Università degli Studi di Modena e Reggio Emilia, Via Vivarelli 10, 41125 Modena, Italy;

*E-mail: federico.croci@unimore.it (F.C)

Abstract. The main purpose of this paper is the development of a CFD modelling methodology for the simulation of alkaline water electrolysis. The growing concern about climate change is pushing more and more countries to facilitate ecological transition programmes. Hydrogen perfectly fits the characteristics to become one of the main actors in many industrial sectors to reduce the emission of polluting gases in hard-to-abate sectors. In this framework, hydrogen must be produced through zero-impact technologies. Alkaline water electrolysis is the most widespread technology to produce green hydrogen, and through its CFD modelling it is possible to accurately simulate the behaviour of these components and enhance their performance. In this study, two three-dimensional models have been created representing two types of alkaline electrolysis cell: the first one is a standard laboratory configuration (wide-gap), the second one is a zero-gap type. Both models are based on a two-phase model (liquid: water and potassium hydroxide electrolyte, gas: hydrogen and oxygen) using a Euler-Euler approach to describe the gas bubble flow. With these models it has been possible to investigate how temperature and electrolyte flow rate affect the production of hydrogen, with particular emphasis on the pressure effect. Increasing the pressure at which hydrogen is produced could mean a significant reduction in storage compression costs, giving new horizons to this technology.

1. Introduction

Climate change and global warming are posing challenging problems to all the governments across the world. The need to decarbonize as much as possible the energy production field is leading to consider more and more renewable sources as a main resource to produce energy. Two of the main problems for this kind of energy production systems are operational intermittence and energy storage. Apart from certain types of hydroelectric power plants that can accumulate water to use it when the energy request is higher and can almost steadily produce renewable electric energy during most days of the year, solar and wind-based plants do not work continuously during the day and usually not at their full load when the request is at its maximum [1]. A way to attenuate such decoupling is to convert the excess of electrical energy into chemical energy by producing green hydrogen with an electrolysis process. Hydrogen can be stored in large quantities, it can be transported and used where and when it is needed the most, allowing to increase the flexibility of renewable energy sources [2][3]. Also, many industrial fields, e.g. chemical industries, use massive amount of hydrogen which is mostly produced through methane steam reforming or coal gasification. Introducing a way to produce it without the emission of pollutant gases would represent a significant step forward for the decarbonization of such sectors. At present, the most widespread and used technologies for green hydrogen production are Proton Exchange Membrane Water Electrolysis (PEMWE) and Alkaline Water Electrolysis (AWE). The

first one is based on a solid thin electrolyte coupled with two electrodes in a Membrane Electrode Assembly (MEA). It can operate at high current densities between $0.6 - 2.0\ A/cm^2$ for less than $2\ V$, resulting in a better efficiency ($60\% - 80\%$) and a higher hydrogen output [4][5]. The main disadvantage for this technology is the usage of platinum group metal material (PGM) and iridium oxide as catalyst especially in the anodic oxygen evolution, which leads to much more expensive components. That is why the most common water electrolysis process is AWE. Using a liquid electrolyte, usually potassium hydroxide (KOH) or sodium hydroxide (NaOH), it does not require precious metal as catalyst for the semi-reaction, the electrodes are usually made of nickel (Ni) leading to a much cheaper electrolysis cell. As consequences, the performance in AWE is lower than in PEMWE with a range of current densities of $0.2 - 0.6\ A/cm^2$ for voltages of $1.8 - 2.4\ V$, so more energy is required to obtain the same hydrogen output [6][7]. However, being a more developed technology guarantees longer lifetime, which combined with lower costs justifies its mainstream use. In recent years the renewed interest for AWE has led to the development of many studies on the state of the art and on the creation of multidimensional models. Hu et al. [6] reported an accurate review of AWE, comparing it with other electrolysis technologies, giving indication on how many operational parameters affects the cell performances and providing a mathematical model to simulate it. Zeng et al. [8], starting by exhaustively describing the AWE technology, showed in detail the most recent progresses regarding electrodes composition and electrolytes additives in order to improve the cell efficiency. The focus of many studies has been concentrated on how to model and improve overpotential losses in particular activation and ohmic losses in the main components of an AWEC [9][10]. For the zero-gap type of cell (porous electrodes, no gap between solid parts) the growth of bubbles on electrode surfaces has a big impact on performances. Kadyk et al. [11] studied a way to enhance the gas removal from porous electrodes, concluding that sacrificial sites for bubble nucleation in the electrodes can significantly improve cell performances. Schllings et al. [12] have modelled how forced flow can influence the bubble removal and the results have shown many advantages using forced convection. Lee et al. [13] have developed a precise 3D numerical model to study how gas evolution processes, temperature, and inlet velocity of the electrolyte affect the performance of a zero-gap AWEC based on experimental data. No articles were found that studied different geometries configuration of cells and, most important, just a few took care of how pressure changes can influence cell performances [14][15], but without using 3D CFD analysis on a cell level. For these reasons the focus of this paper is to investigate the behaviour of alkaline water electrolysis cells (AWEC) through 3D CFD models using COMSOL Multiphysics, validated against experimental and numerical literature data. With these models the temperature, inlet velocity and pressure sensitivities are deeply investigated to reach a better understanding of the process to improve AWEC performance.

1.1 Alkaline Water Electrolysis

In **figure 1** a schematic AWE is shown. An alkaline solution, containing KOH in our case, is introduced to both anode and cathode by external forced circulation. It allows the migration of OH^- ions from the negative to the positive electrode. Electrical energy is supplied thanks to an external generator and splits liquid water molecules into gaseous hydrogen and oxygen through the following semi-reactions taking place on the surfaces of two electrodes:

$$\text{Cathode}\quad 2H_2O + 2e^- \rightarrow 2OH^- + H_2 \quad E^0_{NE} = -0.828\ V \tag{1}$$

$$\text{Anode}\quad 2OH^- \rightarrow H_2O + \frac{1}{2}O_2 + 2e^- \quad E^0_{PE} = 0.4011\ V \tag{2}$$

Where E_{PE}^{0} and E_{NE}^{0} represent the thermodynamics equilibrium potential of the oxygen and hydrogen evolution reaction (OER and HER, respectively).
The complete reaction for the AWE process can be written as:

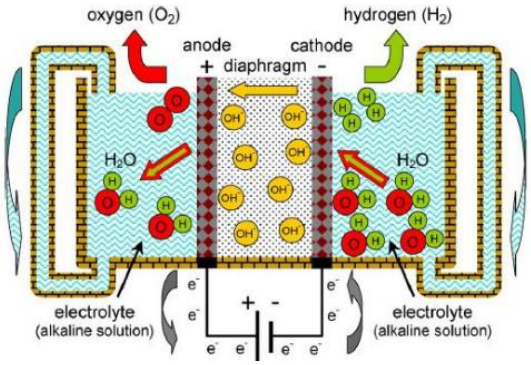

Figure 1. Basic AWE cell, components, chemical and transport processes [20].

$$H_2O \rightarrow H_2 + \frac{1}{2}O_2 \tag{3}$$

As mentioned, the AWEC works with medium-low current densities due to high voltage losses that results in poor efficiencies for working points with $i > 1\ A/cm^2$. Hence, despite being a well-known and developed technology, it has many areas where it can be improved via simulations.

2. Mathematical Model

A three-dimensional AWEC model is based on two coupled modules: one for the description of the electrochemical processes developing in the cell, and one for the two-phase flow evolution. The second one consists in a Euler-Euler mixture approach where the interpenetrating continua share the same pressure. Volume fraction for each phase was used since the volume occupied by one phase cannot be occupied by other phases. Also, mass-averaged mixture velocity and diffusive mass flux were considered. In this study the models are simplified by the following assumptions, which are commonly shared with fuel cells modelling [16], [17]:

1. Laminar flow regime of the mixture, because of the low fluid velocity which results in low Reynolds number.
2. Ideal gas behaviour for hydrogen and oxygen which are presumed to be dispersed as gaseous bubbles (dispersed phase, $_d$) in the continuous liquid electrolyte (continuous phase, $_c$).
3. Porous electrodes are isotropic, and transport phenomena can be described by considering effective permeability, uniform porosity and tortuosity.
4. The gravitational force was not considered.
5. Butler–Volmer kinetics govern the electrochemical reaction at the anode and cathode.
6. Bubble adherence to the walls, deformation, circulation and coalescence are neglected.
7. All AWE cells are assumed to be isothermal.

2.1 3D geometry

The 3D geometry is illustrated in **Figure 2**. The dimensions are summarized in **Table 1**.

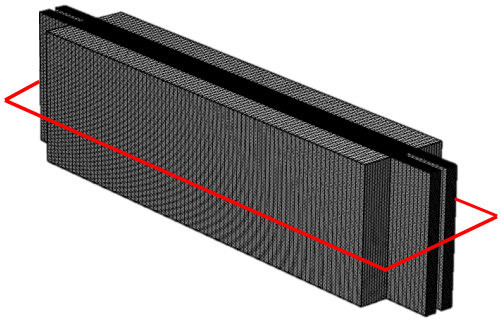

Figure 2. 3D geometry and mesh, with red-marked cross section plane for 2D plots.

Table 1. Cells dimensions.

Name	Value	Description
x_{sep}	4.6E-4 m	Separator Thickness
x_{cell}	0.0018 m	Current Collectors Thickness
A_{cell}	2.16E-4 m^2	Cell Surface
x_{el}	7E-4 m	Electrodes Thickness
y_{cell}	0.027 m	Cell Width
z_{cell}	0.008 m	Cell Height

Even though they remain the same for both zero and wide gap configurations, the zero-gap cell uses two porous electrodes made of nickel that physically connects current collectors and separator, while the wide-gap cell has two nickel electrodes idealized as planar surfaces attached to the bipolar plates, so, there is gap filled with the electrolyte between electrodes and separator.

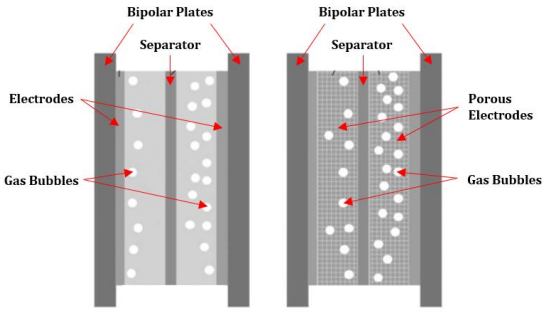

Figure 3. Wide-gap configuration (left), zero-gap configuration (right) [21].

The operating conditions for both cells are summarized in **Table 2**. The liquid electrolyte is introduced at both anode and cathode with the same velocity.

Table 2. Operating condition, from [13].

Name	Value	Description
T_{cell}	353 K	Cell temperature
p_{gas}	1 atm	Inlet pressure
v_{in}	0.1 m/s	Electrolyte inlet velocity
$C_{KOH,in}$	6724.992 mol/m^3	KOH inlet concentration
$C_{H2O,in}$	48818 mol/m^3	H_2O inlet concentration

2.2 Electrochemical model

The COMSOL "Water Electrolyzer" module was used to model all the most important electrochemical equations. The voltage that has to be applied to the cell to sustain the process as it is calculated by the software is represented in expression (4):

$$V(i) = E_{eq,PE/NE} + \left(V_{act,PE}(i) + V_{act,NE}(i)\right) + V_{ohm,sep}(i) + V_{ohm,PE}(i) + V_{ohm,NE}(i) + V_{bubble}(i) \quad (4)$$

The Butler-Volmer equation was used to express the local current density i at both positive (PE) and negative (NE) electrodes:

$$i_{NE} = \varepsilon_{liquid} A_{v,NE}\, i_{0,NE} \left[\left(\frac{C_{OH^-}}{C_{OH^-}^{ref}}\right)^2 \left(\frac{C_{H_2}}{C_{H_2}^{ref}}\right) exp\left(\frac{\alpha_a F \eta_{NE}}{RT_{cell}}\right) - \left(\frac{C_{H_2O}}{C_{H_2O}^{ref}}\right)^2 exp\left(\frac{-\alpha_c F \eta_{NE}}{RT_{cell}}\right) \right] \quad (5)$$

$$i_{PE} = \varepsilon_{liquid} A_{v,PE}\, i_{0,PE} \left[\left(\frac{C_{OH^-}}{C_{OH^-}^{ref}}\right)^2 exp\left(\frac{\alpha_a F \eta_{PE}}{RT_{cell}}\right) - \left(\frac{C_{O_2}}{C_{O_2}^{ref}}\right)^{1/2} \left(\frac{C_{H_2O}}{C_{H_2O}^{ref}}\right) exp\left(\frac{-\alpha_c F \eta_{PE}}{RT_{cell}}\right) \right] \quad (6)$$

Where ε_{liquid} is the electrolyte volume fraction. $A_{v,NE}$ and $A_{v,PE}$ represents the ratios between electrochemical active surface and the total volume of the porous electrode, α_a and α_c are the anodic and cathodic transfer coefficients, and η_{PE} and η_{NE} denotes the superficial overpotentials, similarly to the model implemented in [18]. The terms $i_{0,PE}$ and $i_{0,NE}$ represents the exchange current densities for the oxygen electrode reaction (OER) and for the hydrogen electrode reaction (HER) and they were defined as function of temperature with the following expressions:

$$i_{0,PE/NE} = i_{o,ref,PE/NE} \cdot \exp\left[\frac{-E_{a,PE/NE}}{R}\left(\frac{1}{T_{cell}} - \frac{1}{T_{ref}}\right)\right] \quad (7)$$

Here $E_{a,PE}$ and $E_{a,NE}$ denote the activation energies for the reactions at the anode and at the cathode, respectively, while $i_{o,ref,PE}$ and $i_{o,ref,NE}$ are the reference value for the exchange current densities. For the thermodynamics reference potential of the OER and HER the following expression was used:

$$E_{eq,ref,PE/NE}(T) = E^0 + \frac{\Delta s_{PE/NE}}{2F}(T_{cell} - T_0) \quad (8)$$

In these equations Δs_{PE} and Δs_{NE} express the entropy variations during the reactions at anode and cathode. From that it is possible to calculate the equilibrium potentials at both positive and negative electrodes using the Nernst equation as follows:

$$E_{eq,PE/NE} = E_{eq,ref,PE/NE}(T) - \frac{RT}{nF} ln \prod_i \left(\frac{p_i}{p_{i,ref}}\right)^{\nu_i} \quad (9)$$

The governing equations for the multi-phase flow implemented with this module are represented in **Table 3**.

Table 3. Governing equations for the multiphase flow implemented via "Water Electrolyzer module".

Name	Equation	Terms
Charge transport solid media	$\nabla \cdot \boldsymbol{i}_s = -i_{v,total}$	$\boldsymbol{i}_s = -\sigma_{s,eff} \nabla \boldsymbol{\phi}_s$
Charge transport Electrolyte	$\nabla \cdot \boldsymbol{i}_l = i_{v,total}$	$\boldsymbol{i}_l = -\sigma_{l,eff} \nabla \boldsymbol{\phi}_l$
Maxwell-Stefan species transport	$\rho \frac{\partial}{\partial t}(\omega_i) + \rho(u \cdot \nabla)\omega_i = \nabla \cdot \left(\rho \omega_i \sum_{k=1}^{Q} D_{ik,eff} d_k + D_i^T \frac{\nabla T}{T} \right) + R_i$	Ref. [22]

The effective ionic conductivity in all porous media was calculated using the tortuosity correlation:

$$\sigma_{l,eff} = \frac{\varepsilon}{\tau} \sigma_l \quad (10)$$

Where ε represent the porosity and τ is the tortuosity of the porous materials.
For the effective electrical conductivity in porous electrodes the Zamel [19] correlation was used:

$$\sigma_{s,eff} = \sigma_s \cdot \left\{ 1 - 0.962 \cdot \left(\frac{3\varepsilon}{2-\varepsilon} \right) \cdot exp[0.889 \cdot (1-\varepsilon)] \cdot (1-\varepsilon)^{-0.00715} \right\} \quad (11)$$

While for the bipolar plates made of SS304 and for the Zirfon separator the electrical conductivity values were taken from [13]. Starting from the data in [13] the diffusion coefficient for hydrogen and oxygen was defined with the following equations:

$$D_{ik} = D_{ik,ref}\ exp\left[-\frac{E_{a,i}}{R} \left(\frac{1}{T_{cell}} - \frac{1}{T_{ref}} \right) \right] \quad (12)$$

Here, the subscript *i* stands for *i-th* species and *k* for the *k-th* phase. After that, the effective value was calculated via the Bruggeman correlation as follows:

$$D_{ik,eff} = D_{ik} \varepsilon^{\tau} \varepsilon_{gas}^{(\tau-1)} \quad (13)$$

In which ε_{gas} denote the gas volume fraction.
The hydrogen production mass flow rate was calculated using the Faraday law:

$$\dot{N}_{H_2} = \frac{i_{NE} \cdot A_{cell} \cdot MW_{H2}}{2F} \quad (14)$$

The power supplied to the cell was given by equation (15):

$$P_{el} = V(i) \cdot i_{NE} \cdot A_{cell} \quad (15)$$

2.3 Euler-Euler model for two-phase mixture flow

To complete the model physics the "Euler-Euler Model, Laminar Flow" interface was used. It allows to implement the continuity and momentum equations, described in **Table 4**, where the continuous phase is the liquid electrolyte, while the dispersed phases are gaseous hydrogen at the cathode and oxygen at the anode. In this way the gas development can be modelled in a

Table 4. Governing equations for the multiphase flow implemented via "Euler-Euler model, Laminar flow".

Name	Equation	Terms
Continuity equation for continuous phase	$\frac{\partial}{\partial t}(\rho_c\phi_c) + \nabla * (\rho_c\phi_c\boldsymbol{u}_c) = m_{dc}$	Ref. [23]
Continuity equation for dispersed phase	$\frac{\partial}{\partial t}(\rho_d\phi_d) + \nabla * (\rho_d\phi_d\boldsymbol{u}_d) = -m_{dc}$	Ref. [23]
Momentum equation for continuous phase	$\rho_c\phi_c\left[\frac{\partial}{\partial t}(\boldsymbol{u_c}) + \boldsymbol{u_c}\nabla(\boldsymbol{u_c})\right] = -\phi_c\nabla p + \phi_c\nabla * \tau_c + \boldsymbol{F}_{m,c} + \phi_c\boldsymbol{F}_c + m_{dc}(\boldsymbol{u}_{int} - \boldsymbol{u}_c)$	Ref. [23]
Momentum equation for dispersed phase	$\rho_d\phi_d\left[\frac{\partial}{\partial t}(\boldsymbol{u_d}) + \boldsymbol{u_d}\nabla(\boldsymbol{u_d})\right] = -\phi_d\nabla p + \phi_d\nabla * \tau_d + \boldsymbol{F}_{m,d} + \phi_d\boldsymbol{F}_d + m_{dc}(\boldsymbol{u}_{int} - \boldsymbol{u}_d)$	Ref. [23]

comprehensive way. Assuming Newtonian fluids, the stress tensor for continuous and dispersed phases can be described as in equations (16-17):

$$\tau_c = \mu_c^m\left(\nabla\boldsymbol{u}_c + (\nabla\boldsymbol{u}_c)^T - \frac{2}{3}(\nabla\cdot\boldsymbol{u}_c)\boldsymbol{I}\right) \quad (16)$$

$$\tau_d = \mu_d^m\left(\nabla\boldsymbol{u}_d + (\nabla\boldsymbol{u}_d)^T - \frac{2}{3}(\nabla\cdot\boldsymbol{u}_d)\boldsymbol{I}\right) \quad (17)$$

where μ_{mix} is the dynamic viscosity of the mixture and it was calculated with a "volume average" model:

$$\mu_{mix} = \phi_c\mu_c + \phi_d\mu_d \quad (18)$$

$$\mu_c^m = \mu_d^m = \mu_{mix} \quad (19)$$

ϕ is the volume fraction of and μ is dynamic viscosity for each phase.

The interphase momentum transfer was defined with the term F_i that represents the sum of drag, lift and bubble dispersion forces, respectively, as described in equation (18):

$$\boldsymbol{F}_i = -\frac{3}{4}\phi_d\rho\frac{C_d}{d_{bubble}}|\boldsymbol{u}_{slip}|\boldsymbol{u}_{slip} - \phi_d\rho C_l|\boldsymbol{u}_{slip}|\nabla * \boldsymbol{u}_c - \phi_d\rho\frac{K_d}{d_{bubble}}|\boldsymbol{u}_{slip}|\nabla\phi_d \quad (20)$$

Where the slip velocity is defined as:

$$\boldsymbol{u}_{slip} = \boldsymbol{u}_d - \boldsymbol{u}_c \quad (21)$$

C_l represent the lift coefficient, d_{bubble} is the average bubble diameter and K_d is the gas dispersion factor. To calculate the drag coefficient the Shiller-Naumann drag model was implied:

$$C_d = \begin{cases} \frac{24}{Re_p}\left(1 + 0.15Re_p^{0.687}\right) & Re_p < 1000 \\ 0.44 & Re_p > 1000 \end{cases} \quad (22)$$

The inlet velocity is low, so the Reynolds number, calculated like in expression (23), is lower than 1000.

$$Re_p = \frac{d_d \rho_c |\boldsymbol{u}_{slip}|}{\mu_c} \quad (23)$$

3. Results

The validation of the mathematical model was achieved by comparing the experimental and simulation data on the polarization curve reported in [13] to the data obtained with the 3D simulation of the zero-gap configuration. As visible in **Figure 4-5**, the mathematical model results follow the polarization curves of the simulation presented in [13] and, as consequences, the experimental data.

The increasing in voltage losses when the working temperature decreases are caused by the drop of the exchange current density and of the effective diffusion coefficient, as highlighted by

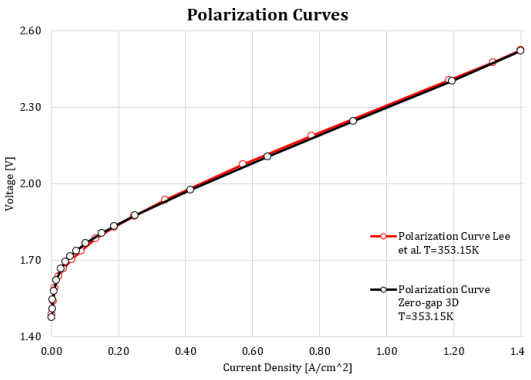

Figure 4. Polarization curves for model validation at T=353.15 K.

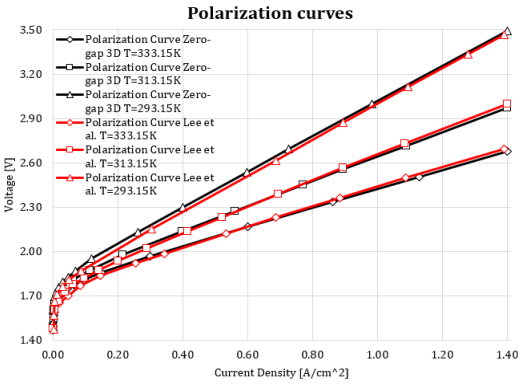

Figure 5. Polarization curves for model validation at T=333.15 K, T=313.15 K and T=293.15 K.

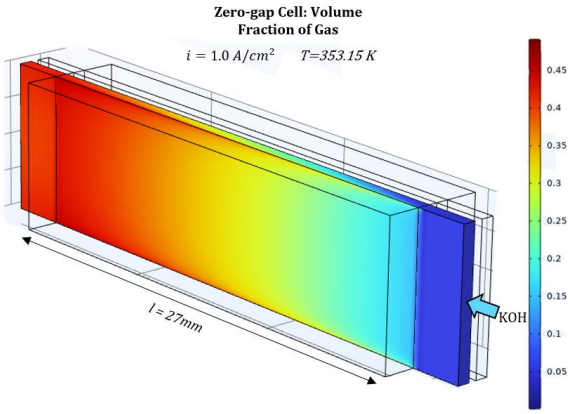

Figure 6. Volume fraction of hydrogen distribution through the cell.

equations (7)(12). Combined with the reduction of electrolyte and overall separator conductivity, the cell performance significantly decreases as the temperature reduces. As visible in **Figure 7** for

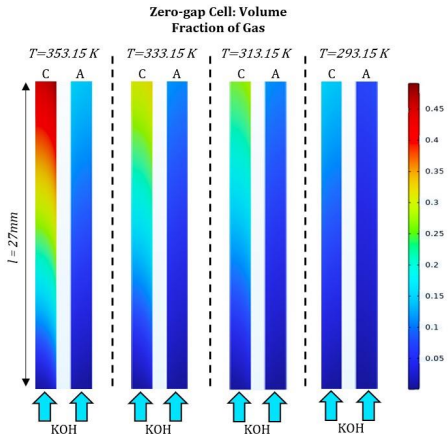

Figure 7. Zero-gap cell Temperature sensitivity: volume fraction of gas at *i=1.0 A/cm²*.

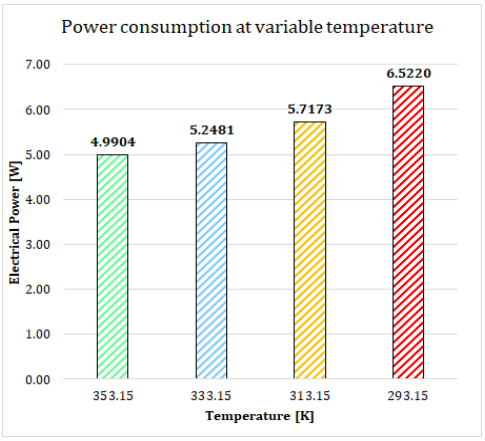

Figure 8. Zero-gap cell Temperature sensitivity: single cell power consumption at *i=1.0 A/cm²*.

$i = 1.0\ A/cm^2$ the volume fraction of hydrogen at cathode increases from inlet to outlet due to hydrogen generation, although it decreases moving to lower operating temperature because of the higher overpotentials. This leads to higher electrical power supplied to the cell in order to achieve the same hydrogen production rate, as shown in **Figure 8**. Comparing the results for the zero-gap cell at different current densities ($i = 0.5\ A/cm^2$ and $i = 1.0\ A/cm^2$) (**Figure 9**) it is noticeable the increment in hydrogen and oxygen production at the cost of higher ohmic and concentration losses, where for the first case $\dot{N}_{H_2} = 1.13054E-8\ kg/s$, while for $i = 1.0\ A/cm^2$ $\dot{N}_{H_2} = 2.26104E-8\ kg/s$. Also, the electrolyte velocity slightly increases due to the bubble obstruction of pores in the central part of the negative electrode.

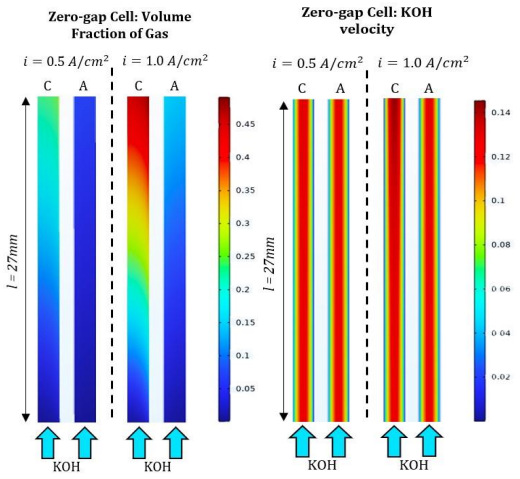

Figure 9. Zero-gap cell comparison at different

Afterward, the sensitivity to the electrolyte flow rate was investigated considering two other inlet velocity in addition to the initial one ($v_{in} = 0.01\ m/s$ and $v_{in} = 0.4\ m/s$). The results are shown in **Figure 10-11**, where for a flow rate reduction by a factor of 10 ($v_{in} = 0.01\ m/s$) the cell performance decreases significantly at medium-high current densities. This means that the gas

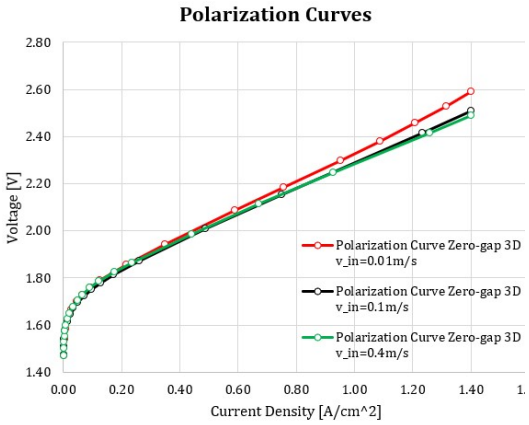

Figure 10. Polarization curves: v_{in} sensitivity.

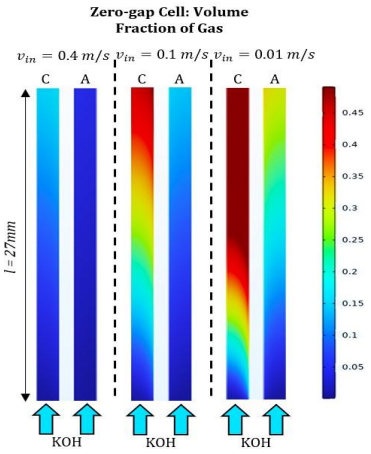

Figure 11. Zero-gap cell v_{in} sensitivity: volume fraction of gas at $i = 1.0\ A/cm^2$.

evacuation given by the insufficient electrolyte flow rate cannot keep up with the nucleation and growth of hydrogen bubbles sticking on the electrode surface reducing the active area and lowering the ionic conductivity of the electrolyte, leading to higher concentration and ohmic overpotentials with a 1% increase in power consumption for the cell considered for $i = 1.0\ A/cm^2$. By contrast, if the inlet velocity is increased 4 times ($v_{in} = 0.4\ m/s$) the volume fraction of gas in the porous electrodes decreases, resulting in marginally lower overpotentials.

In view of the relevance of high-pressure gaseous hydrogen storage, its production at high pressure could sensibly reduce the compression power and cost needed. For this reason, a simulation considering a 90 *bar* pressure at both anode and cathode was carried out and the polarization curve is shown in **Figure 12**.

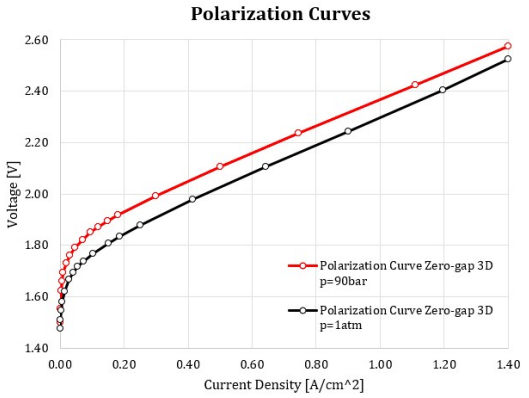

Figure 12. Polarization curves: pressure sensitivity.

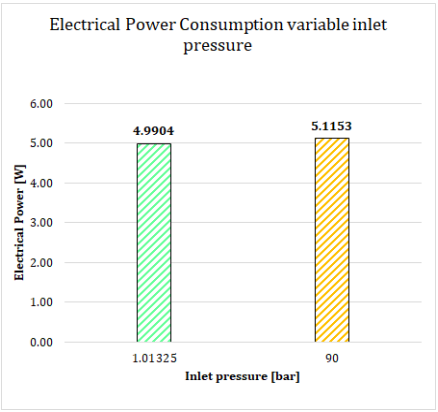

Figure 13. Zero-gap cell Pressure sensitivity: single cell power consumption at *i=1.0 A/cm²*.

Increasing the pressure of the products means a rise in activation overpotential, as explained in equation (9). However, the ohmic overpotentials are lower than in the atmospheric pressure cell likewise in reference [14]. The production rate of hydrogen decreases under equal voltage. As consequences to reach the same hydrogen mass flow at the outlet section the consume of electrical power increases (**Figure 13**). Although, considering the energy saved in the compression phase during storage, the overall efficiency of the full production plant could benefit from producing hydrogen at a higher pressure.
Finally, a comparison between the two types of cells was made. **Figure 14** shows how the wide-

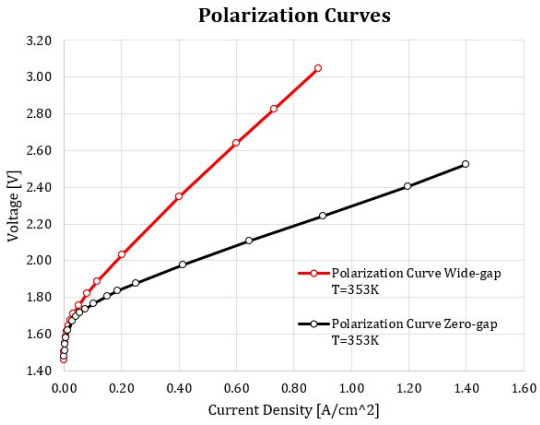

Figure 14. Polarization curves comparison wide-gap zero-gap cells.

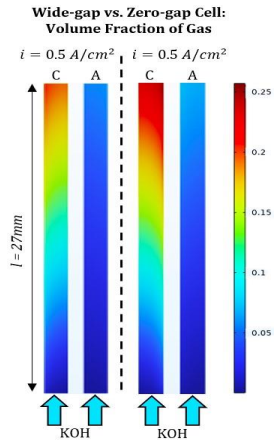

Figure 15. Comparison wide-gap zero-gap cells: volume fraction of gas.

gap configuration has considerably worse performances than the zero-gap. The wide-gap cell suffers from a physical distance between the electrodes, resulting in a long path for the ion conduction and leading to high ohmic losses. Therefore, a wide-gap AWEC is limited to operate with low current densities as testified in [6], while a zero-gap configuration reaches higher current densities resulting in better performance and efficiency. The required power to attain the same production at $i = 0.5\ A/cm^2$ is greater than 17% in comparison with the zero-gap configuration.

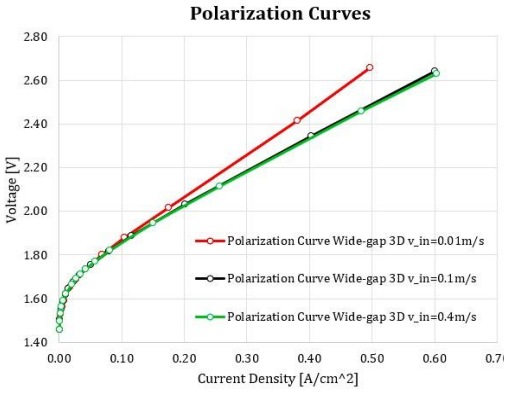

Figure 16. Wide-gap cell: v_{in} sensitivity.

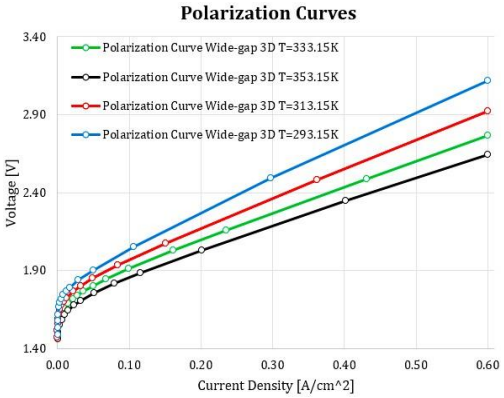

Figure 17. Wide-gap cell: Temperature sensitivity.

For the wide-gap cell the same sensitivities were investigated and the results **Figures 16-17** lead to almost the same consideration already mentioned.

Conclusions

In this study, three-dimensional two-phase models were developed using an electrochemical module coupled with a Euler-Euler mixture approach to simulate AWEC with two different geometries: zero- and wide-gap. These models were successfully validated against literature and simulation data for voltages up to 2.6 V and current densities up to 1.4 A/cm^2. The excellent agreement between the model results and the literature data continues for different operating temperature confirming the quality of the presented model. The simulation results accurately predict the behaviour of the cells at different temperatures, flow rates and pressure allowing to simulate dissolved and bubble transport of hydrogen and oxygen forecasting the overpotential losses at different operating conditions. Increasing the operating pressure leads to a growth in losses for most of the working range, which means that at the same current density the electrolysis performance is lower reducing the hydrogen production rate, although the savings in power for compression could render it as an attractive solution to lower the hydrogen production and storage cost.

Acknowledgement

The present research work has received financial support from the Italian Ministry of Universities and Research, Project of National Interest, PRIN 2022 - HAWCS "*Hydrogen Advanced Solutions for Water EleCtrolysis and solid-state*", CUP E53D23003220006.

References

[1] L. Lu, H. Yang, and J. Burnett, "Investigation on wind power potential on Hong Kong islands-an analysis of wind power and wind turbine characteristics," 2002. [Online]. Available: www.elsevier.com/locate/renene

[2] A. S. Mehr, A. D. Phillips, M. P. Brandon, M. T. Pryce, and J. G. Carton, "Recent challenges and development of technical and technoeconomic aspects for hydrogen storage, insights at different scales; A state of art review," Jun. 12, 2024, *Elsevier Ltd*. doi: 10.1016/j.ijhydene.2024.05.182.

[3] S. Zhu *et al.*, "Design and optimization of a cascade hydrogen storage system for integrated energy utilization," *J Energy Storage*, vol. 96, Aug. 2024, doi: 10.1016/j.est.2024.112732.

[4] G. Corda, A. Cucurachi, S. Fontanesi, and A. d'Adamo, "Three-Dimensional CFD Simulation of a Proton Exchange Membrane Electrolysis Cell," *Energies (Basel)*, vol. 16, no. 16, Aug. 2023, doi: 10.3390/en16165968.

[5] Z. Ma, L. Witteman, J. A. Wrubel, and G. Bender, "A comprehensive modeling method for proton exchange membrane electrolyzer development," *Int J Hydrogen*

Energy, vol. 46, no. 34, pp. 17627–17643, May 2021, doi: 10.1016/j.ijhydene.2021.02.170.

[6] S. Hu *et al.*, "A comprehensive review of alkaline water electrolysis mathematical modeling," *Appl Energy*, vol. 327, Dec. 2022, doi: 10.1016/j.apenergy.2022.120099.

[7] A. S. Emam, M. O. Hamdan, B. A. Abu-Nabah, and E. Elnajjar, "A review on recent trends, challenges, and innovations in alkaline water electrolysis," Apr. 25, 2024, *Elsevier Ltd*. doi: 10.1016/j.ijhydene.2024.03.238.

[8] K. Zeng and D. Zhang, "Recent progress in alkaline water electrolysis for hydrogen production and applications," Jun. 2010. doi: 10.1016/j.pecs.2009.11.002.

[9] M. T. de Groot and A. W. Vreman, "Ohmic resistance in zero gap alkaline electrolysis with a Zirfon diaphragm," *Electrochim Acta*, vol. 369, Feb. 2021, doi: 10.1016/j.electacta.2020.137684.

[10] J. W. Haverkort and H. Rajaei, "Voltage losses in zero-gap alkaline water electrolysis," *J Power Sources*, vol. 497, Jun. 2021, doi: 10.1016/j.jpowsour.2021.229864.

[11] T. Kadyk, D. Bruce, and M. Eikerling, "How to Enhance Gas Removal from Porous Electrodes?," *Sci Rep*, vol. 6, Dec. 2016, doi: 10.1038/srep38780.

[12] J. Schillings, O. Doche, and J. Deseure, "Modeling of electrochemically generated bubbly flow under buoyancy-driven and forced convection," *Int J Heat Mass Transf*, vol. 85, pp. 292–299, 2015, doi: 10.1016/j.ijheatmasstransfer.2015.01.121.

[13] J. Lee, A. Alam, C. Park, S. Yoon, and H. Ju, "Modeling of gas evolution processes in porous electrodes of zero-gap alkaline water electrolysis cells," *Fuel*, vol. 315, May 2022, doi: 10.1016/j.fuel.2022.123273.

[14] D. Jang, H. S. Cho, and S. Kang, "Numerical modeling and analysis of the effect of pressure on the performance of an alkaline water electrolysis system," *Appl Energy*, vol. 287, Apr. 2021, doi: 10.1016/j.apenergy.2021.116554.

[15] F. Khalighi, N. G. Deen, Y. Tang, and A. W. Vreman, "Hydrogen bubble growth in alkaline water electrolysis: An immersed boundary simulation study," *Chem Eng Sci*, vol. 267, Mar. 2023, doi: 10.1016/j.ces.2022.118280.

[16] A. D'Adamo, M. Haslinger, G. Corda, J. Höflinger, S. Fontanesi, and T. Lauer, "Modelling Methods and Validation Techniques for CFD Simulations of PEM Fuel Cells," *Processes 2021, Vol. 9, Page 688*, vol. 9, no. 4, p. 688, Apr. 2021, doi: 10.3390/PR9040688.

[17] G. Corda *et al.*, "A Methodology to Design the Flow Field of PEM Fuel Cells," *SAE Int J Adv Curr Pract Mobil*, vol. 5, no. 6, pp. 2078–2092, Apr. 2023, doi: 10.4271/2023-01-0495.

[18] G. Corda, S. Fontanesi, and A. d'Adamo, "Methodology for PEMFC CFD Simulation Including the Effect of Porous Parts Compression," *Int J Hydrogen Energy*, vol. 47, no. 32, pp. 14658–14673, Apr. 2022, doi: 10.1016/J.IJHYDENE.2022.02.201.

[19] N. Zamel, X. Li, and J. Shen, "Numerical estimation of the effective electrical conductivity in carbon paper diffusion media," *Appl Energy*, vol. 93, pp. 39–44, May 2012, doi: 10.1016/J.APENERGY.2011.08.037.

[20] R. Fang and Y. Liang, "Control strategy of electrolyzer in a wind-hydrogen system considering the constraints of switching times," *Int J Hydrogen Energy*, vol. 44, no. 46, pp. 25104–25111, Sep. 2019, doi: 10.1016/j.ijhydene.2019.03.033.

[21] F. Rocha, R. Delmelle, C. Georgiadis, and J. Proost, "Effect of pore size and electrolyte flow rate on the bubble removal efficiency of 3D pure Ni foam electrodes during alkaline water electrolysis," *J Environ Chem Eng*, vol. 10, no. 3, Jun. 2022, doi: 10.1016/j.jece.2022.107648.

[22] "Multicomponent Gas Diffusion: Maxwell–Stefan Description." Accessed: May 22, 2024. [Online]. Available: https://doc.comsol.com/5.6/doc/com.comsol.help.battery/battery_ug_chemsptrans.09.147.html

[23] "The Euler–Euler Model Equations." Accessed: May 22, 2024. [Online]. Available: https://doc.comsol.com/6.1/doc/com.comsol.help.cfd/cfd_ug_fluidflow_multi.09.153.html#2396757